Advanced Functional Materials

ADVANCED FUNCTIONAL MATERIALS
www.afm-journal.de

RESEARCH ARTICLE

Atomic-Level Interstitial Engineering Programs Sub-Bandgap States for Energetically Matched Charge Transfer in $Cs_3Bi_2Cl_9$ Enabling Selective and Sensitive H_2S Sensing

Keke Li[1] | Wenwen Zhang[1] | Shujia Wang[1] | Zhida Gao[1] | Yan-Yan Song[1] | Junjian Zhao[2]

[1]College of Sciences, Northeastern University, Shenyang, P. R. China | [2]Department of Pharmacy, Shenyang Medical College, Shenyang, P. R. China

Correspondence: Zhida Gao (gaozd@mail.neu.edu.cn) | Yan-Yan Song (yysong@mail.neu.edu.cn) | Junjian Zhao (jjzhao@symc.edu.cn)

Received: 25 November 2025 | **Revised:** 5 January 2026 | **Accepted:** 13 January 2026

Keywords: energetic charge-transfer alignment | interstitial defect engineering | lead-free halide perovskites | selective molecular interaction | sub-bandgap states

ABSTRACT

Constructing energetically matched charge-transfer pathways between molecules and solid-state materials is essential for achieving selective interfacial reactions, yet remains challenging at room temperature. Here, we introduce an atomic-level electronic-structure modulation strategy in which Cu^+ interstitials are incorporated into lead-free $Cs_3Bi_2Cl_9$, generating Cu-3d-dominated sub-bandgap states that act as efficient electronic intermediates. These tailored states narrow the bandgap, increase the local density of states, and achieve near-resonant alignment ($\Delta E \approx 0.11$ eV) with the redox level of H_2S, establishing a highly favorable charge-transfer pathway. Using H_2S as a model molecule, the optimized $Cu_{0.10}$-CBC exhibits intrinsically selective interaction, enabling a ppt-level theoretical limit of detection (730 ppt), an experimentally validated detection limit of 5 ppb, fast response/recovery (50/90 s), and excellent stability over 125 days. In situ DRIFTS spectroscopy, DFT calculations, and Bader charge analysis reveal that interstitial Cu simultaneously serves as a high-affinity adsorption center and electron-pumping site, promoting molecular activation and interfacial redox conversion. Flexible $Cu_{0.10}$-CBC devices further maintain robust performance under mechanical deformation and enable accurate breath-H_2S quantification. This work establishes a generalizable sub-bandgap engineering paradigm for programming charge-transfer energetics in halide perovskites, offering a materials-centric foundation for selective chemical interfaces and low-power sensing technologies.

1 | Introduction

Understanding and controlling molecule–solid charge transfer is essential for applications ranging from heterogeneous catalysis to chemical interfaces and wearable diagnostics [1–3]. A central challenge lies in constructing energetically aligned electronic states that can selectively couple with specific molecular redox levels at room temperature [4–6]. Most solid-state materials possess intrinsically fixed band structures, limiting their ability to host tailored sub-bandgap states or mediate molecule-specific electron exchange [7–10]. As a result, achieving selective and low-energy molecular recognition-particularly at room temperature-remains difficult.

Lead-free halide perovskites offer an attractive platform for electronic-structure engineering due to their defect-tolerant lattices, soft ionic bonding, and rich defect chemistry [11–13]. Their tunable band edges and ability to stabilize diverse intrinsic or

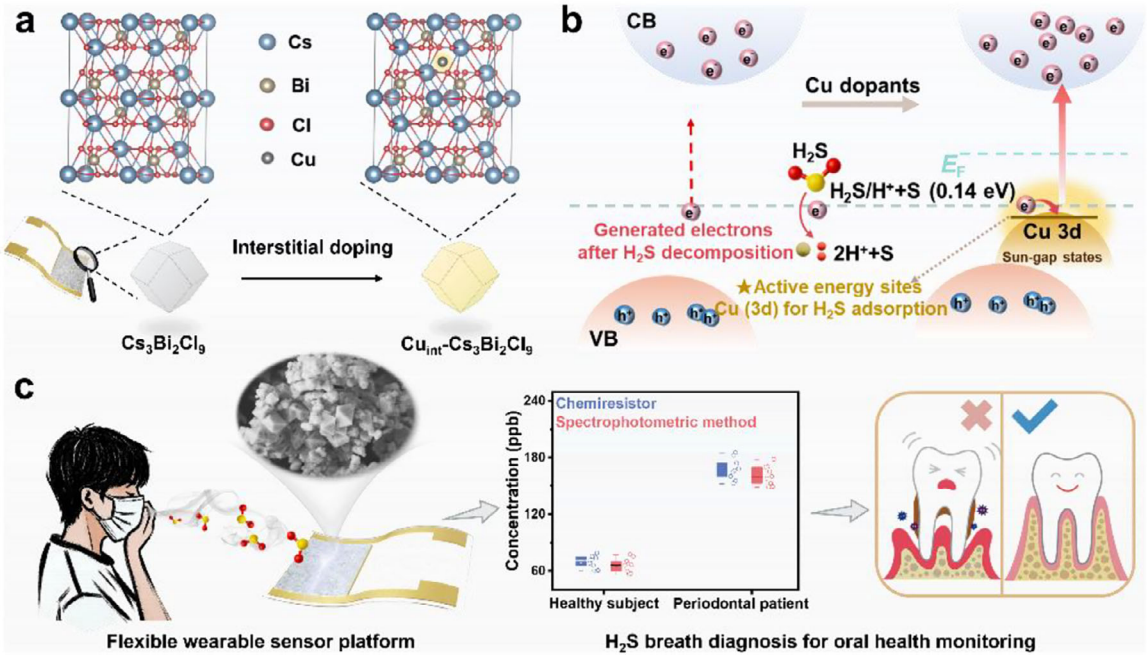

FIGURE 1 | Schematic illustration of (a) the fabrication process of the Cu_{int}-$Cs_3Bi_2Cl_9$ (Cu_{int}-CBC)–based flexible gas sensor, (b) the proposed H_2S sensing mechanism driven by Cu-interstitial–induced sub-bandgap states, and (c) the noninvasive H_2S breath diagnosis for oral health monitoring.

extrinsic defects provide a fertile basis for programming interfacial charge-transfer pathways [14–16]. However, conventional halide perovskites often display ambipolar responses toward oxidizing and reducing species [17–19], and efforts to enhance selectivity through heterostructures, external stimuli, or sensor arrays usually increase system complexity. This raises a broader materials question: can we engineer perovskite electronic structures to intrinsically match specific molecular redox levels and thereby direct selective charge transfer?

In catalysis and photocatalysis, band-structure modulation and defect engineering are widely employed to tune reaction energetics by aligning electronic states with key intermediates [20, 21]. Translating these principles to molecular recognition requires designing sub-bandgap states that are both energetically accessible and chemically active [22–24]. Interstitial dopants, in particular, can generate highly localized electronic states, alter local symmetry, and introduce additional charge-transfer channels [25, 26]. Yet, achieving atomic-level control over interstitial configurations and their energetic alignment with target molecules remains largely unexplored in halide perovskites.

Here, we establish an atomic-level interstitial-engineering strategy in which Cu^+ ions are incorporated into $Cs_3Bi_2Cl_9$ (CBC) to create Cu-3d–dominated sub-bandgap states that fundamentally reshape the charge-transfer landscape (Figure 1a). First-principles calculations and spectroscopic analyses reveal that interstitial Cu dopants: i) narrow the bandgap and enrich localized electronic density; ii) introduce well-defined sub-gap states, and iii) create a near-resonant energetic alignment ($\Delta E \approx 0.11$ eV) with the redox level of H_2S (Figure 1b). This near-resonant alignment leads to an energetically favorable electron-transfer channel and simultaneously enhances H_2S adsorption via strong Cu-S affinity [24–26]. Using H_2S as a model system, the optimized $Cu_{0.10}$–CBC material exhibits intrinsically selective charge-transfer behavior at room temperature, offering ultralow detection limits, rapid dynamics, and excellent long-term stability. Flexible devices further demonstrate robust performance under mechanical deformation and accurate quantification of breath-borne H_2S (Figure 1c). By revealing the dual function of Cu interstitials-as high-affinity adsorption centers and electron-pumping intermediates-this work establishes a generalizable sub-bandgap engineering paradigm for programming charge-transfer energetics in lead-free halide perovskites, providing a materials-centric foundation for selective chemical interfaces and next-generation low-power sensing technologies.

2 | Result and Discussion

2.1 | Structural Evolution and Sub-Bandgap Formation Via Cu Doping

To establish the structural foundation of our sub-bandgap engineering strategy, the effect of Cu interstitial doping on modulating the crystal framework and electronic environment of CBC were managed. As conceptually illustrated in Figure 1, Cu incorporation plays three synergistic roles: introducing Cu-3d-dominated sub-bandgap states that narrow the bandgap and increase the local density of states, creating an energetically matched charge-transfer channel with the reduction potential of H_2S; functioning as an electron-pumping center that accelerates interfacial electron exchange; and enhancing H_2S adsorption and activation through intrinsic Cu-S affinity.

Lead-free Cu_x-CBC perovskites were synthesized via a modified acidic precipitation method [27, 28], yielding phase-pure crystals without the need for inert-atmosphere protection. The detailed synthesis route was provided in the Experimental Section and Figure S1. The crystal structures of CBC and Cu_x-CBC are

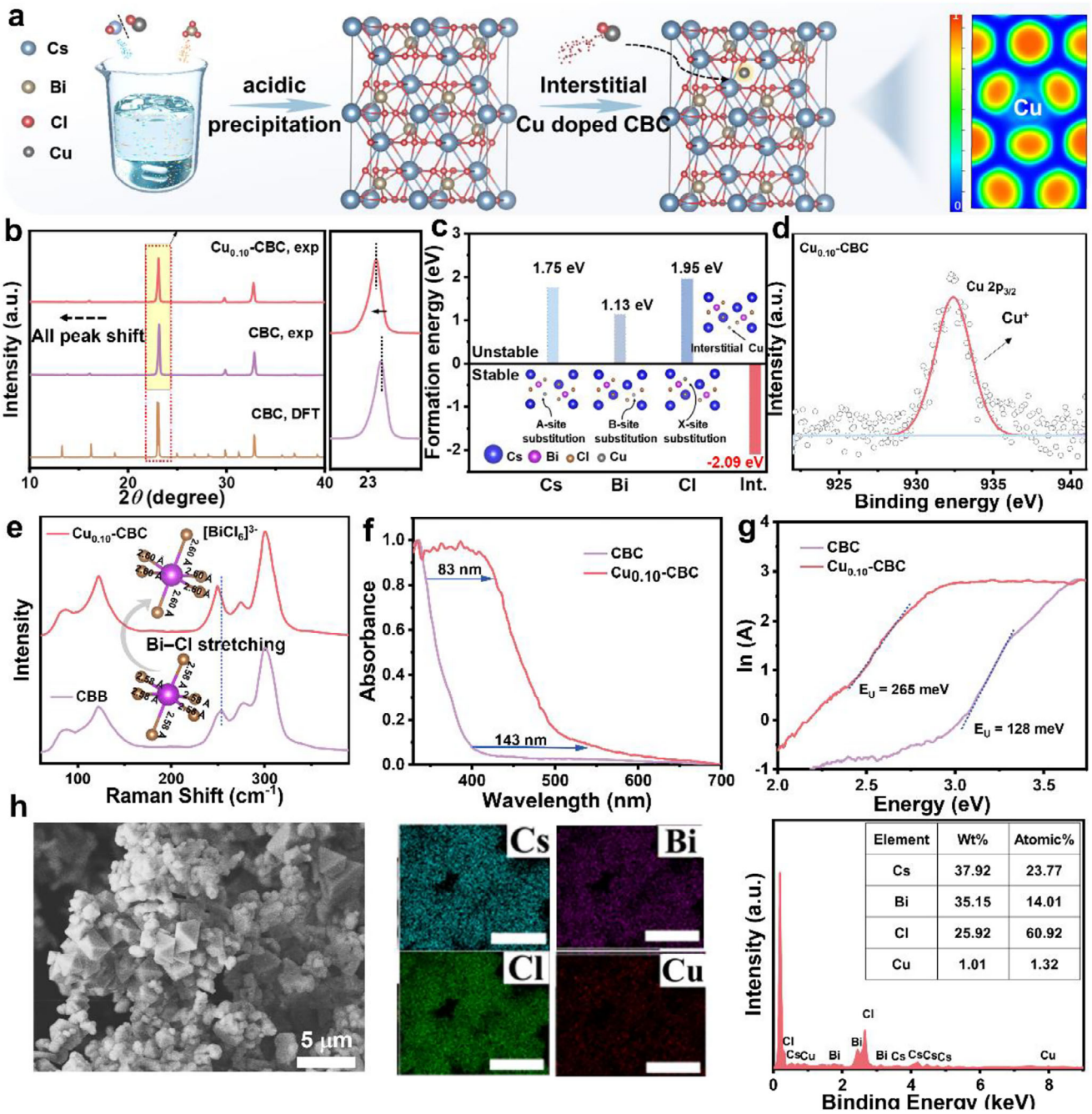

FIGURE 2 | (a) Schematic illustration of the preparation of $Cs_3Bi_2Cl_9$ (CBC) incorporating interstitial Cu dopants. Cs, Bi, Cl, and Cu atoms are depicted as blue, khaki, red, and gray spheres, respectively. The right panel presents the corresponding 2D charge-density distribution. (b) XRD patterns of CBC and $Cu_{0.10}$-CBC, with magnified views of the highlighted regions shown on the right. (c) Formation energies of Cu^+ substitution and interstitial incorporation in the CBC lattice, accompanied by schematic illustrations of the corresponding defect configurations. (d) XPS spectra of the Cu 2p region for $Cu_{0.10}$-CBC. (e) Raman spectra, (f) UV–vis absorption spectra, and (g) extracted Urbach energies of CBC and $Cu_{0.10}$-CBC. (h) SEM image of $Cu_{0.10}$-CBC along with elemental mapping and EDS profiles (weight and atomic percentages).

displayed in Figure 2a. First, starting from the cubic phase of $CsPbCl_3$, its stacking pattern along the (111) direction is observed (Figure S2). When Pb^{2+} is replaced by Bi^{3+}, the valence state difference is compensated by the formation of ordered vacancy layers every two (111) planes, resulting in a vacancy-ordered structure composed of corner-sharing $[BiCl_6]^{3-}$ octahedral double layers [29, 30]. On this basis, Cu doping preferentially occupies these vacancies and interacts with surrounding atoms. In Figure 2b, X-ray diffraction (XRD) patterns demonstrate that these Cu_x-CBC samples retain the pristine CBC phase, with no impurity peaks detected. In addition, the diffraction peaks of the Cu-doped CBC samples exhibit a slight shift toward lower angles, and the magnitude of this shift gradually increases with increasing Cu content (Figure 2b inset; Figure S3), which suggest the lattice expansion [31, 32]. This is fully consistent with ionic radii considerations: Cu^+ (≈77 pm) is substantially smaller than Bi^{3+} (≈103 pm) [27, 30]. To determine the specific position of Cu atoms in the CBC structure, we analyzed the two possible

scenarios based on first-principles DFT calculations: (1) located at interstitial sites; and (2) substitutional sites where Cu may replace Cs^+, Bi^{3+}, or Cl^- in the CBC lattice. As shown in Figure 2c, when Cu occupies Cs^+, Bi^{3+}, or Cl^- sites, its formation energy (F_{form}) is positive, indicating that this configuration reduces structural stability. In contrast, the formation energy for interstitial doping is negative, implying that it is energetically more favorable, thus providing greater stability. These results are consistent with the negative shift of the diffraction peaks in XRD results, confirming that Cu primarily exists in the form of interstitial doping in CBC.

X-ray photoelectron spectroscopy (XPS) further verifies successful Cu incorporation, with the Cu $2p_{3/2}$ peak centered at 932.4 eV (Figure 2d) characteristic of Cu^+ [27, 32]. The slight shifts in Cs 3d, Bi 4f, and Cl 2p core levels (Figure S4) indicate interstitial Cu dopants interact with neighboring atoms, leading to an increase in binding energy [27, 31]. This localized chemical environment change may, to some extent, regulate the adsorption and activation of H_2S molecules on the Cu-CBC catalyst surface. Raman analysis shows that Cu doping does not introduce new vibrational modes (Figure 2e), but the slight shifts in peak positions indicate that the doping alters the local environment of the main lattice (Figure S5) [25, 31]. Optical measurements provide clear evidence of Cu-induced sub-bandgap formation. It can be seen that the absorption edge redshifts significantly from 367 nm (CBC) to ~510 nm for $Cu_{0.10}$-CBC (Figure 2f). Furthermore, Tauc plot analysis reveals that the bandgap decreases from 3.04 to 2.45 eV, respectively (Figure S6). In addition, the introduction of Cu dopants induces prominent sub-bandgap states, as evidenced by a significant increase in Urbach energy and a more pronounced absorption tail in the low-energy region (Figure 2g). The Urbach energy increases from 128 to 265 meV, reflecting enhanced structural disorder and a higher density of localized electronic states. The formation of Cu-3d–related sub-bandgap states is suggested, which may play a meaningful role in adjusting the sensing energetics.

In Figure 2h and Figure S7, SEM images reveal microcrystals (~5–10 μm), with Cu doping inducing a slight increase in particle size. Energy-dispersive X-ray spectroscopy (EDS) mapping confirms the uniform distribution of Cs, Bi, Cl, and Cu within the crystal. Meanwhile, EDS quantification and ICP-MS analysis confirm that the actual Cu content closely matches nominal compositions (Table S1), demonstrating the consistency and controllability of the doping process. The combined experimental and DFT results indicate that Cu^+ dopants preferentially occupy interstitial sites, introducing localized chemical-environment perturbations and generating sub-bandgap states that reshape the electronic landscape.

2.2 | Selective and Ultrasensitive H_2S Detection

H_2S was selected as a probe molecule to elucidate the structure–reactivity relationship of the Cu_x-CBC perovskites under RT and ambient-light conditions (Figure 3a). Gas-sensing measurements were performed using a two-probe configuration, in which the sample-coated flexible interdigitated electrodes were exposed to controlled H_2S concentrations supplied by a precise gas-analysis platform (Figures S8–S10). Upon Cu incorporation, the Cu_x-CBC sensors exhibit a distinctly enhanced response toward H_2S, accompanied by rapid and fully reversible resistance recovery once the atmosphere is switched back to clean air (Figure 3b). A quantitative comparison of response/recovery dynamics and detection limits for the Cu_x-CBC series is presented in Figure 3c. Notably, interstitial Cu plays a decisive role in boosting the sensing capability of CBC. Among all compositions, $Cu_{0.10}$-CBC delivers the optimal performance, featuring a well-defined linear response over the low-concentration range of 0.005–0.2 ppm, with an exceptionally low theoretical detection limit of 730 ppt calculated via RMSD analysis (Figures S11 and S12) [33, 34]. Under exposure to 1 ppm H_2S, $Cu_{0.10}$-CBC achieves fast response/recovery times of 50.9/90.3 s, outperforming pristine CBC (70.2/140.2 s) (Figure 3d; Figure S13).

Remarkably, even in the absence of light irradiation, $Cu_{0.10}$-CBC maintains a measurable response of 1.71 toward 100 ppb H_2S (Figure S14). Such an excellent H_2S-sensing performance in the absence of light can be attributed to the crucial "electron-pumping" function of interstitial Cu in facilitating charge transfer. However, excessive Cu loading (3.6 wt.%) induces a pronounced upward shift of the VBM (Figures S6 and S15), which intensifies carrier recombination and substantially deteriorates the sensing performance [35–37]. This finding highlights the importance of finely tuned interstitial-doping concentrations to balance electronic modulation and charge-transfer efficiency.

To evaluate the selectivity of $Cu_{0.10}$-CBC under complex atmospheric environments, its responses toward H_2S were examined under both single-gas (Figure 3e; Figure S16) and mixed-gas conditions (Figure S17). Distinct from pristine CBC, $Cu_{0.10}$-CBC delivers a sharply defined and dominant response to H_2S, while exhibiting nearly negligible signals toward common interferents. The correlation heat map (Figure 3f) further visualizes this behavior, which reveals an absence of correlation between interfering gases but a strong, exclusive correlation with H_2S, verifying its outstanding selectivity. This exceptional selectivity originates from two synergistic factors: 1) the strong intrinsic affinity between Cu and S, which accelerates gas–surface binding kinetics and enriches the density of active adsorption sites [26, 38]; and 2) the Cu^+ interstitial dopants introduce well-defined sub-gap states that energetically match the reduction potential of H_2S, thereby promoting rapid electron transfer and establishing an efficient charge-transport pathway at the sensing interface [24]. The cyclic sensing stability of $Cu_{0.10}$-CBC was examined over seven consecutive cycles, during which the resistance–time curves remained nearly unchanged (Figure S18), demonstrating remarkable operational robustness. Moreover, ten independently fabricated batches of $Cu_{0.10}$-CBC sensors exhibited a relative standard deviation (RSD) of merely 3.39% at 100 ppb H_2S (Figure S19), confirming excellent device-to-device reproducibility. Long-term stability tests revealed that the sensor retained 91.8% of its initial response even after 125 days of storage (Figure 3g; Figure S20). This excellent durability largely attributed to the suppression of lattice ion migration enabled by interstitial Cu doping, which preserves structural integrity and electrical stability [39, 40]. To further verify the long-term structural and chemical stability of the Cu-doped CBC material, the sensing films were scraped from the devices after gas-sensing tests and characterized by XRD and XPS (Figures S21 and S22). Only weak S 2p signals (~168.5 eV) associated with surface sulfide-like species were detected, with no new XRD peaks observed, indicating negligible bulk

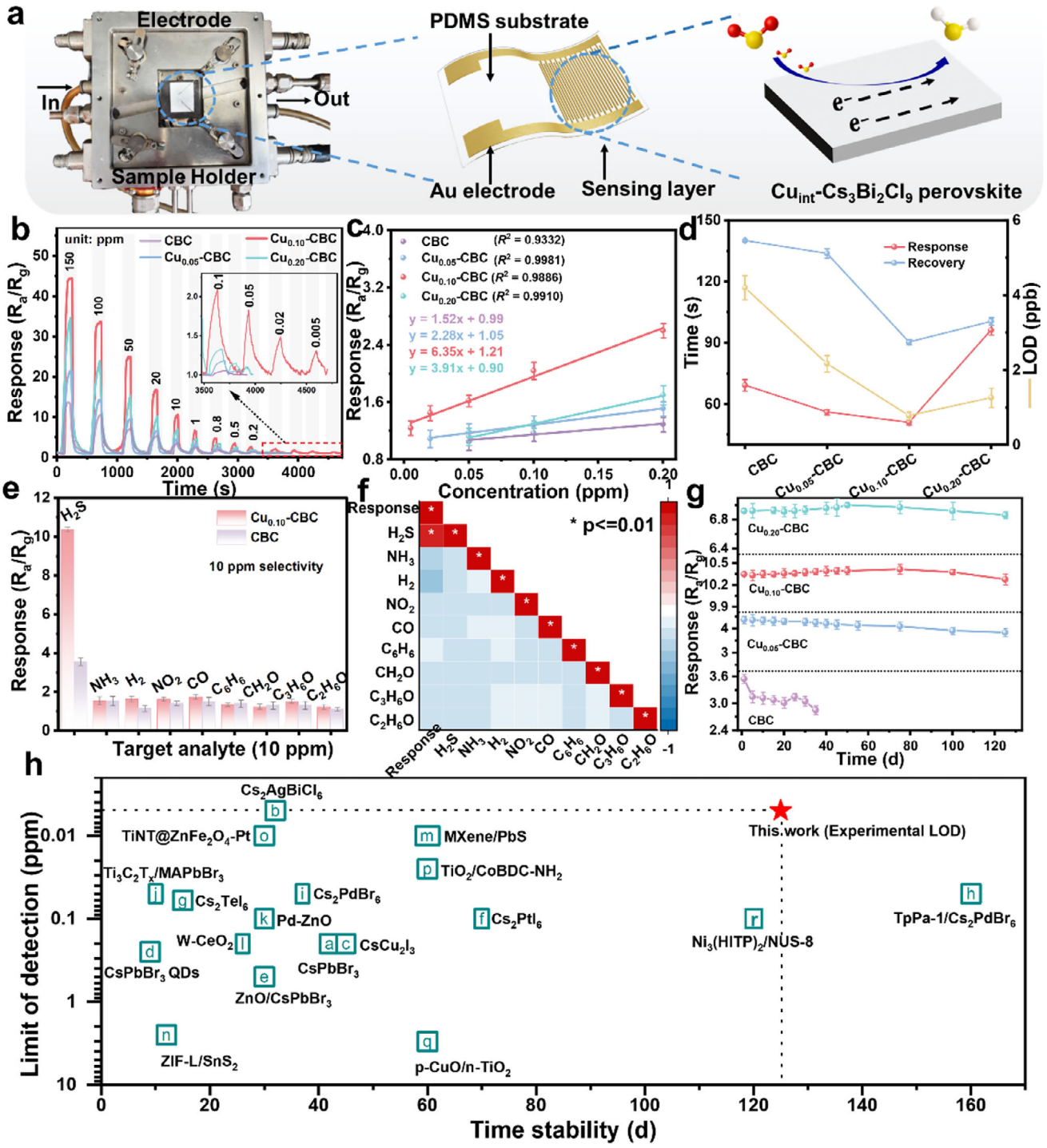

FIGURE 3 | (a) Schematic and optical photographs of the Cu_{int}-CBC gas sensors. (b) Real-time response curves of Cu_x-CBC sensors toward H_2S over concentrations ranging from 5 ppb to 150 ppm. (c) Linear fitting of the response-concentration relationship within the 0.005–0.2 ppm range. (d) Comparison of response times, recovery times, and lower limits of experimental detection (LOD). (e) Selectivity evaluation against various interfering gases (NO_2, SO_2, NH_3, H_2, acetone, benzene, formaldehyde, and ethanol, all at 10 ppm). (f) Correlation heat map of $Cu_{0.10}$-CBC sensor responses to mixed gases ($P < 0.01$). (g) Long-term stability of the $Cu_{0.10}$-CBC sensor toward 10 ppm H_2S at RT. (h) Comparison of experimentally measured LOD and long-term stability with recently reported resistive gas sensors. Number of individual experiments, $n = 3$.

sulfide formation. The preserved crystal structure confirmed the excellent structural stability of the Cu-doped CBC sensor. The humidity stability of $Cu_{0.10}$-CBC was further assessed (Figures S23 and S24). Its H_2S response remained essentially unchanged with increasing relative humidity, indicating excellent robustness. This tolerance arose from interstitial Cu–induced electronic-structure modulation, where Cu-3d–dominated sub-bandgap states introduced effective charge-transfer pathways and local electron enrichment suppressed competitive H_2O adsorption (Figure S25) [41, 42]. Thus, preferential H_2S activation and charge transfer

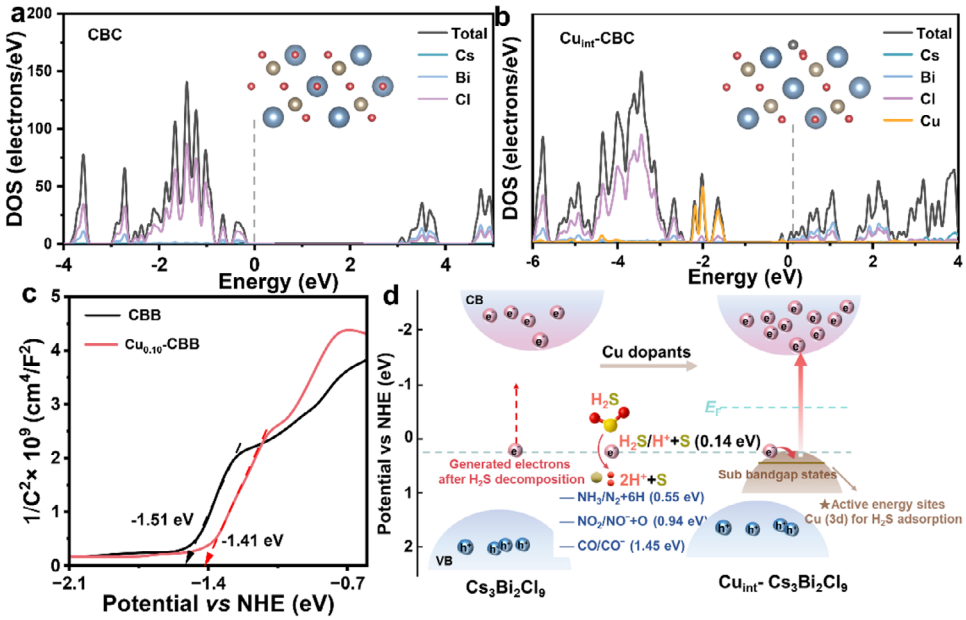

FIGURE 4 | (a) Density of states (DOS) of pristine CBC and (b) $Cu_{0.10}$-CBC showing the emergence of Cu-induced sub-bandgap states. (c) Mott–Schottky plots of CBC and $Cu_{0.10}$-CBC. (d) Schematic band alignment and comparison of the reduction potentials of various gases with the H_2S reduction potential.

were preserved even under humid conditions. Additionally, the sensor exhibited only slight performance fluctuations with varying temperature, demonstrating good thermal stability and practical applicability (Figure S26). The resulted $Cu_{0.10}$-CBC integrates low-temperature operation, exceptional selectivity, rapid response/recovery, and remarkable long-term stability-achieving a level of performance that surpasses most previously reported perovskite- and MOS-based gas sensors (Figure 3h; Table S2).

2.3 | Electronic–Interfacial Mechanism of Cu-Interstitial–Boosted H_2S Sensing

To investigate the origin of the significantly enhanced H_2S response induced by interstitial Cu doping, density functional theory (DFT) calculations were conducted to examine the electronic structures of CBC before and after Cu incorporation. As shown in Figure 4a,b, Cu doping effectively narrows the bandgap between the valence band maximum (VBM) and conduction band minimum (CBM), while simultaneously introducing pronounced sub-gap states originating primarily from Cu 3d orbitals (Figure 4b). These Cu-derived sub-bandgap states markedly increase the local charge density and enable more efficient carrier transport pathways [27, 35], thereby reducing the energy required for VB→CB transitions and supplying additional electronic channels favorable for gas–solid charge exchange [24, 43]. Such electronically optimized states underpin the excellent room-temperature sensing performance of $Cu_{0.10}$-CBC. To further clarify the intrinsic correlation between electronic structure and sensing activity, the flat-band potentials of CBC and $Cu_{0.10}$-CBC were measured by Mott–Schottky analysis (Figure 4c). Relative to the normal hydrogen electrode (NHE), the VBM potentials of CBC and $Cu_{0.10}$-CBC are 1.53 and 1.04 V, respectively, while their CBM potentials are −1.51 and −1.41 V. Based on these parameters, as shown in Figure 4d, the corresponding band diagrams reveal an exceptionally small energy offset of only 0.11 eV between the H_2S reduction potential and the Cu-induced sub-bandgap level. This near-resonant alignment greatly accelerates electron transfer from H_2S to the Cu-modified perovskite surface, directly contributing to the enhanced responsivity and high selectivity observed experimentally.

To elucidate the gas–solid interaction at the atomic scale, DFT calculations were further performed to assess the adsorption energetics and interfacial electronic structures toward H_2S and various other gases, supported by Bader charge analysis (Figure 5). A fully optimized $Cu_{0.10}$-CBC surface model was constructed with all possible adsorption sites considered (Figure 5a; Figure S27). The results demonstrate that H_2S preferentially binds to Cu sites with an adsorption energy of −1.43 eV (Figure 5a), confirming that interstitial Cu dopants serve as strong chemisorption centers. Moreover, the adsorption energies toward common interfering gases are significantly weaker (Figure 5a; Figures S28 and S29), consistent with the experimentally observed selectivity (Figure 3e,f). Charge density difference (CDD) mapping (Figure 5b) reveals substantial electron redistribution around the Cu-H_2S interface [44]. Bader charge analysis indicates that each H_2S molecule transfers 0.109 e to the $Cu_{0.10}$-CBC surface, providing direct evidence of strong electronic coupling responsible for the sensing response [45, 46]. This electron transfer trend is consistent with the 2D charge distribution shown in Figure 5c. Additionally, DOS calculations reveal a slight shift of electronic states toward lower energy upon H_2S adsorption (Figure 5d,e), together with an increase in the density of states near the Fermi level-further confirming electron injection from H_2S and the subsequent reorganization of surface energy levels [43]. These findings collectively verify that interstitial Cu doping fundamentally enhances the affinity and selectivity of CBC toward H_2S.

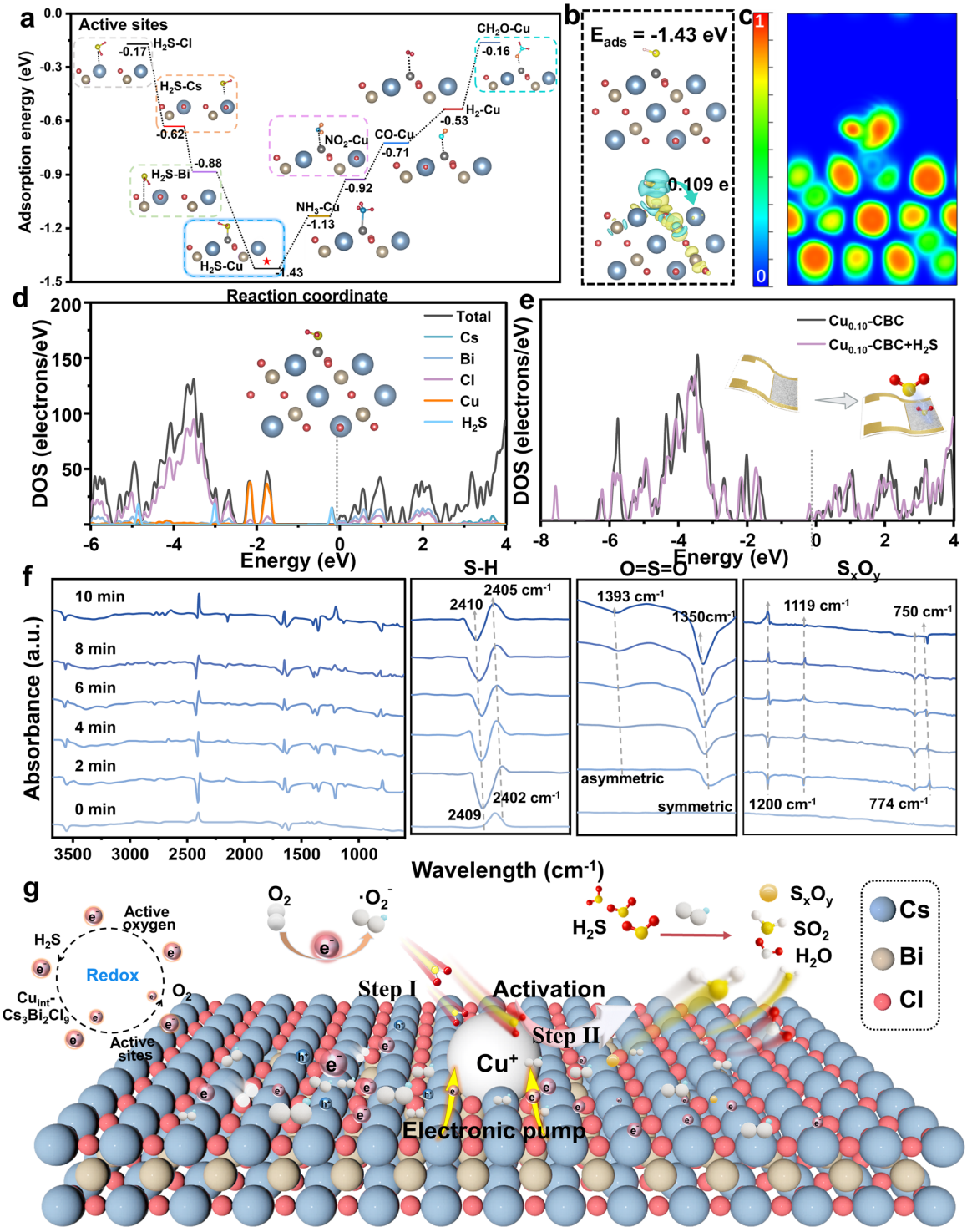

FIGURE 5 | (a) Adsorption energies of H_2S and various interfering gases on different active sites of $Cu_{0.10}$-CBC. (b) Charge-density-difference map of $Cu_{0.10}$-CBC, where yellow and blue regions indicate electron accumulation and depletion, respectively. (c) 2D charge distribution of $Cu_{0.10}$-CBC. (d,e) DOS of $Cu_{0.10}$-CBC before and after H_2S adsorption. (f) In situ DRIFTS spectra of $Cu_{0.10}$-CBC under H_2S exposure at room temperature. (g) Schematic illustration of the $Cu_{0.10}$-CBC structural model and the proposed H_2S sensing mechanism.

The adsorption and catalytic oxidation processes were further explored using in situ DRIFTS (Figure 5f). Following H_2S introduction, a characteristic S—H stretching vibration at 2403–2411 cm^{-1} immediately appears, indicating the formation of HS^- intermediates. As the reaction proceeds, progressively intensified absorbances at 1344–1382 cm^{-1} (O═S═O asymmetric stretching), 1086–1120 cm^{-1} (O═S═O/S═O symmetric stretching) [47], and 900–1100 cm^{-1} (S-O vibrations) signal the rapid oxidation of H_2S into higher-valence sulfites and sulfates [48]. The band variations in the 700–1200 cm^{-1} region reflect the dynamic evolution of intermediate S_xO_y species [49]. Altogether, the DRIFTS results confirm a sequential conversion route of $H_2S \rightarrow HS^- \rightarrow$

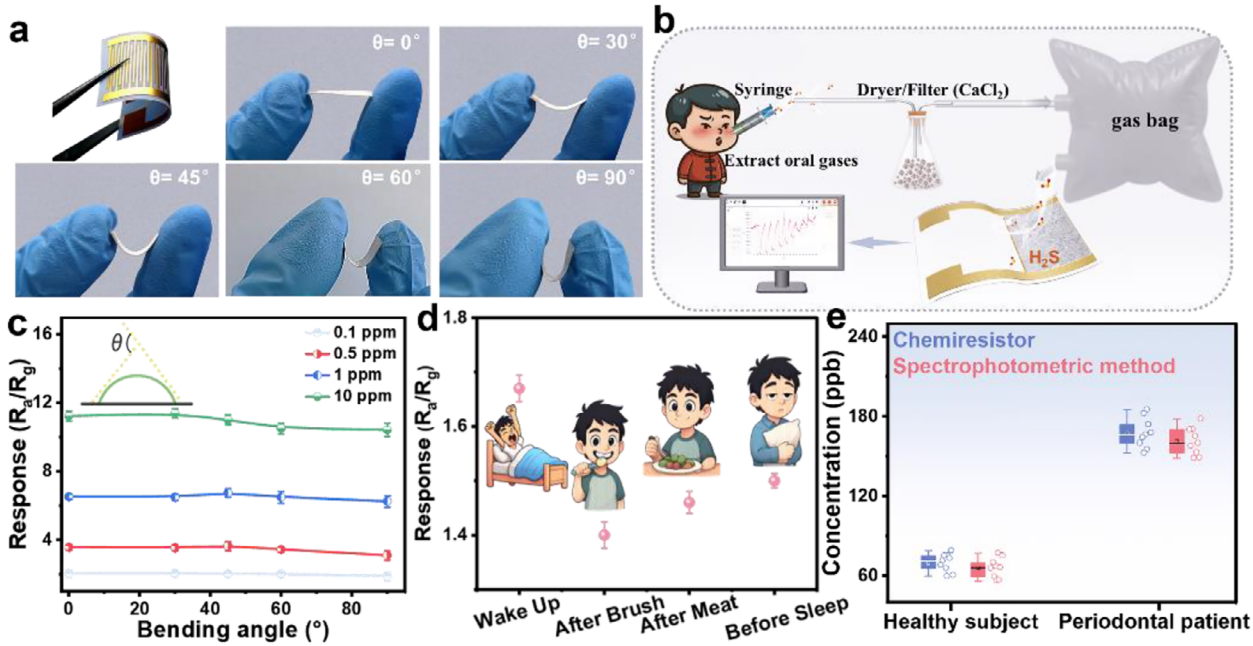

FIGURE 6 | (a) Schematic illustration of the flexible $Cu_{0.10}$-CBC sensor under different bending angles. (b) Schematic of the breath-sampling system for oral gas collection. (c) Response stability of the flexible $Cu_{0.10}$-CBC sensor under various bending conditions. (d) Sensor responses to exhaled breath collected at different daily time points (upon waking, after brushing teeth, after eating, and before sleep). (e) Comparison of H_2S concentrations in exhaled breath from healthy individuals and periodontitis patients measured using the $Cu_{0.10}$-CBC sensor and spectrophotometric method ($n = 9$). Number of individual experiments, $n = 3$.

SO_2/S_xO_y (Equations (1) and (2)) [50–52]. In contrast, these vibrational features are substantially weaker for pristine CBC (Figure S30), underscoring the decisive role of interstitial Cu in promoting both adsorption and catalytic oxidation processes.

$$O_{2(ads)} + e^- \rightarrow O_2^-(ads) \quad (1)$$

$$2H_2S_{(ads)} + 3O_2^- \rightarrow 2H_2O_{ads} + 2SO_2 + 3e^- \quad (2)$$

The above theoretical and spectroscopic analyses reveal that interstitial Cu ions endow CBC with a dual-function enhancement: i) Cu sites act as high-affinity adsorption and electron-transfer centers, and ii) Cu-derived sub-bandgap states enable precise energetic matching with the redox level of H_2S. This synergy dramatically improves charge-transfer kinetics, thereby delivering the outstanding responsivity, selectivity, and long-term stability of the $Cu_{0.10}$-CBC gas-sensing device at low operating temperatures (Figure 5g).

2.4 | Flexible and Wearable H_2S Sensing Device

To assess the practical applicability of the $Cu_{0.10}$-CBC-based sensor, a flexible device was fabricated on a 100 μm-thick PET substrate. The mechanical robustness of the device was evaluated by bending it to various angles and measuring its response to multiple H_2S concentrations (100, 500 ppb, 1, and 10 ppm). As shown in Figure 6a,c, and Figure S31, the sensor maintains stable output even under bending angles up to 90°, and after 200 bending cycles at 45°, only a negligible decrease in response is observed. These results confirm that the $Cu_{0.10}$-CBC sensing layer retains excellent structural and functional integrity under repeated deformation, underscoring its strong potential for wearable gas-sensing applications.

To further explore its utility in real-world health monitoring, exhaled breath from volunteers was collected at different daily time points (after waking up, tooth brushing, lunch, and before bedtime) using 10 mL sampling bags (Figure 6b). A dehumidification module was placed at the inlet to remove moisture interference before the breath samples were introduced into the testing chamber. As shown in Figure 6d and Figure S32, the average response immediately after waking was 1.68, corresponding to an H_2S concentration of approximately 74.02 ppb based on the calibration curve in Figure 3c. This value aligns well with previously reported morning H_2S levels in human breath [53, 54]. After tooth brushing, lunch, and before bedtime, the H_2S concentrations were determined as 29.92, 39.37, and 45.66 ppb, respectively. Since tongue coating is the primary source of H_2S in the oral cavity, effective oral cleaning markedly lowers its concentration. Clinically, an exhaled H_2S level above 100 ppb is commonly regarded as an indicator of pathological halitosis, while patients with periodontal disease can exhibit concentrations exceeding 150 ppb [54, 55]. To validate the accuracy of the $Cu_{0.10}$-CBC sensor, H_2S levels in breath from both healthy individuals and periodontal-disease patients were analyzed using the methylene blue spectrophotometric method alongside sensor measurements (Figure S33). As shown in Figure 6e, the H_2S concentrations measured by the $Cu_{0.10}$-CBC sensor closely agree with those obtained from the methylene blue spectrophotometric analysis, demonstrating the high analytical precision and reliability of this sensor for noninvasive oral health assessment via breath monitoring.

3 | Conclusion

In conclusion, we demonstrate that interstitial Cu doping provides an effective pathway to engineer sub-bandgap states in $Cs_3Bi_2Cl_9$, enabling selective and energy-matched charge transfer with H_2S molecules. This tailored electronic structure endows $Cu_{0.10}$−CBC with exceptional room-temperature sensing performance, including ppt-level detection, rapid response/recovery, and long-term operational stability. Combined theoretical and spectroscopic analyses reveal that Cu ions function simultaneously as high-affinity adsorption sites and electron-transfer mediators, establishing the fundamental origin of the material's superior selectivity. Furthermore, the flexible $Cu_{0.10}$−CBC device exhibits excellent mechanical durability and reliably quantifies H_2S in human breath, aligning closely with clinical reference measurements. This work highlights interstitial-dopant engineering as a powerful and generalizable strategy for developing high-performance, low-power perovskite gas sensors for future wearable and diagnostic applications.

4 | Experimental Section

4.1 | Synthesis of CBC

The $Cs_3Bi_2Cl_9$ was synthesized with slight modifications to a previously reported method [31], as schematically shown in the Figure S1. In detail, a mixture of 3 mmol CsCl and 2 mmol $BiCl_3$ was dissolved in 3 mL of 10 M HCl solution, stirred at 75°C for 30 min to yield a pale white precipitate. The precipitate was subsequently filtered, washed four times with ethanol, and dried at 100°C overnight. The $Cs_3Bi_2Cl_9$ is denoted as CBC.

4.2 | Preparation of Cu-Doped CBC

0.05, 0.1, and 0.2 mL of 0.1 M CuCl solution were added to the mixed solution. The mixture was then stirred for an additional 30 min to ensure complete reaction, and the precipitates were collected by filtration. The resulting products were designated as $Cu_{0.05}$-CBC, $Cu_{0.10}$-CBC, and $Cu_{0.20}$-CBC, respectively.

4.3 | Statistical Analysis

All quantitative experiments and measurements were conducted using at least three independently fabricated samples, and the results are presented as mean ± standard deviation (SD). Error bars represent ±SD ($n = 3$). Origin (Microcal) was employed for data visualization, histogram construction, curve fitting, and graph presentation. The VESTA package was used for structural visualization, and density functional theory (DFT) calculations were performed using the Vienna Ab initio Simulation Package (VASP, v5.4.1).

Acknowledgements

This work was supported by the National Natural Science Foundation of China, China (No. 22374015); Liaoning Province Foundation for Distinguished Young Scholars, China (No. 1727146584490, to Y.−Y.S.); Fundamental Research Funds for the Central Universities, China (N25QNR014). The PhD Start-up Foundation of Liaoning Province, China (No. 2025-BS-0868). Special thanks are due to the instrumental or data analysis from Analytical and Testing Center, Northeastern University.

Conflicts of Interest

The authors declare no conflicts of interest.

Data Availability Statement

The data that support the findings of this study are available in the supplementary material of this article.

References

1. E. Istif, H. Mirzajani, Ç. Dağ, et al., "Miniaturized Wireless Sensor Enables Real-Time Monitoring of Food Spoilage," *Nature Food* 4 (2023): 427–436.

2. D. Gashnikova, F. Maurer, E. Sauter, et al., "Highly Active Oxidation Catalysts Through Confining Pd Clusters on CeO_2 Nano-Islands," *Angewandte Chemie International Edition* 63 (2024): 202408511.

3. X. Li, C. Luo, Q. Fu, et al., "A Transparent, Wearable Fluorescent Mouthguard for High-Sensitive Visualization and Accurate Localization of Hidden Dental Lesion Sites," *Advanced Materials* 32 (2020): 2000060.

4. F.-Z. Chen, L. Hou, Y. Gao, et al., "Polyoxometalates: Cascading Functionality to Unique On-Off Organic Photoelectrochemical Transistor Operation," *Advanced Functional Materials* 34 (2024): 2408186.

5. Q. Zhang, L. Zhang, X.-N. Liu, et al., "Establishing Interfacial Charge-Transfer Transitions on Ferroelectric Perovskites: An Efficient Route for Photoelectrochemical Bioanalysis," *ACS Sensors* 5 (2020): 3827–3832.

6. J. Zhang, X. Liu, G. Neri, and N. Pinna, "Nanostructured Materials for Room-Temperature Gas Sensors," *Advanced Materials* 28 (2016): 795–831.

7. W. Deng, M. Zhang, C. Li, M. Yao, and G. Xu, "Energy-Level Alignment at TiO_2 @NH_2 -MIL-125 Interface for High-Performance Gas Sensing," *Angewandte Chemie International Edition* 64 (2025): 202419195.

8. J. Kong, N. R. Franklin, C. W. Zhou, et al., "Nanotube Molecular Wires As Chemical Sensors," *Science* 287 (2000): 622–625.

9. B. Yang, N. V. Myung, and T. T. Tran, "1D Metal Oxide Semiconductor Materials for Chemiresistive Gas Sensors: A Review," *Advanced Electronic Materials* 7 (2021): 2100271.

10. S.-Y. Yu, J. Hu, Z. Li, et al., "Metal–Organic Framework Nanofluidic Synapse," *Journal of the American Chemical Society* 146 (2024): 27022–27029.

11. W. Ye, H.-Z. Lin, M. Li, L. Jiang, D. Chen, and J.-M. Lu, "Dimensional Reduction in $Cs_2AgBiBr_6$ Enables Long-Term Stable Perovskite-Based Gas Sensing," *Nature Communications* 16 (2025): 4820.

12. W. Ye, M. Li, G. Li, et al., "Covalent Organic Framework-Enhanced Metal Halide Perovskites for Selective and Sensitive Gas Sensing," *Advanced Functional Materials* 35 (2025): 2418897.

13. K. Zhou, H. Yang, Z. Du, et al., "Ultrahigh Selectivity H2S Gas Sensor Based $CsPbBr_3$ Perovskites via Pb-S Bonding Interaction," *ACS Sensors* 10 (2025): 517–525.

14. S. Zhou, Y. Ma, G. Zhou, et al., "Ag-Doped Halide Perovskite Nanocrystals for Tunable Band Structure and Efficient Charge Transport," *ACS Energy Letters* 4 (2019): 534–541.

15. K. Maeda, M. Eguchi, and T. Oshima, "Perovskite Oxide Nanosheets With Tunable Band-Edge Potentials and High Photocatalytic Hydrogen-Evolution Activity," *Angewandte Chemie International Edition* 53 (2014): 13164–13168.

16. M. Cha, P. Da, J. Wang, et al., "Enhancing Perovskite Solar Cell Performance by Interface Engineering Using $CH_3NH_3PbBr0.9I2.1$ Quantum Dots," *Journal of the American Chemical Society* 138 (2016): 8581–8587.

17. H. Chen, M. Zhang, R. Bo, et al., "Superior Self-Powered Room-Temperature Chemical Sensing With Light-Activated Inorganic Halides Perovskites," *Small* 14 (2018): 1702571.

18. W. Ye, L. Zhao, H.-Z. Lin, et al., "Halide Perovskite Glues Activate Two-Dimensional Covalent Organic Framework Crystallites for Selective NO_2 Sensing," *Nature Communications* 14 (2023): 2133.

19. Y. Zhai, G. Duan, J. Hu, et al., "Device-Level in-Sensor Olfactory Perception System Based on Array of PCBM-$MAPbI_3$ Heterostructure Transistors," *Advanced Functional Materials* 34 (2024): 2406239.

20. G. Horvai, "The Matched Potential Method, a Generic Approach to Characterize the Differential Selectivity of Chemical Sensors," *Sensors and Actuators B: Chemical* 43 (1997): 94–98.

21. P. Ernest, S. Michael, S. Shababa, D. R. James, B. A. Artem, and W. Aron, "Electronic Defects in Metal Oxide Photocatalysts," *Nature Reviews Materials* (2022): 503.

22. Y. Sun, G. Chen, S. Xi, and Z. J. Xu, "Catalytically Influential Features in Transition Metal Oxides," *ACS Catalysis* 11 (2021): 13947–13954.

23. P. Liu, J. Ran, B. Xia, S. Xi, D. Gao, and J. Wang, "Bifunctional Oxygen Electrocatalyst of Mesoporous Ni/NiO Nanosheets for Flexible Rechargeable Zn–Air Batteries," *ACS Nano-micro letters* 12 (2020): 68.

24. H. He, C. Zhao, J. Xu, et al., "Exploiting Free-Standing p-CuO/n-TiO_2 Nanochannels As a Flexible Gas Sensor with High Sensitivity for H_2S at Room Temperature," *ACS sensors* 6 (2021): 3387–3397.

25. G. Korotcenkov, *Handbook of Gas Sensor Materials: Properties, Advantages and Shortcomings for Applications*, Vol. 2, (Springer, 2014).

26. S. Lee, H. Choa, S. Choi, et al., "Turning on Selective H_2S Gas Sensing Activity in Ternary Nickel Tungstate Strongly Correlated Electron System Through Sub-Gap Band Manipulation," *Advanced Functional Materials* 35 (2025): 2425477.

27. N. K. Tailor, S. Singh, N. Singh, et al., "Exploring the Feasibility of Copper Incorporation in Halide Perovskites: Impact on CO_2 Photoreduction Performance," *Advanced Energy Materials* 14 (2024): 2402087.

28. K. Matsuzaki, N. Tsunoda, Y. Kumagai, et al., "Hole-Doping to a Cu(I)-Based Semiconductor With an Isovalent Cation: Utilizing a Complex Defect as a Shallow Acceptor," *Journal of the American Chemical Society* 144 (2022): 16572–16578.

29. H. Lin, S. Talebi, W. MacSwain, V. Vanshika, A. Chakraborty, and W. Zheng, "Tailoring Substitutional Sites for Efficient Lanthanide Doping in Lead-Free Perovskite Nanocrystals With Enhanced Near-Infrared Photoluminescence," *ACS Nano* 19 (2025): 14941–14953.

30. A. Biswas, A. J. E. Rowberg, P. Yadav, et al., "Ag Intercalation in Layered $Cs_3Bi_2Br_9$ Perovskite for Enhanced Light Emission With Bound Interlayer Excitons," *Journal of the American Chemical Society* 146 (2024): 19919–19928.

31. N. K. Tailor, S. Singh, M. A. Afroz, K. K. Pant, and S. Satapathi, "Unraveling the Impact of Cu-Doping in Lead Free Halide Perovskites for Markedly Enhancing Photocatalytic CO_2 Reduction Performance," *Applied Catalysis B: Environmental* 340 (2024): 123247.

32. F. Ji, Y. Huang, F. Wang, et al., "Near-Infrared Light-Responsive Cu-Doped $Cs_2AgBiBr_6$," *Advanced Functional Materials* 30 (2020): 2005521.

33. P. Bulemo, D. Kim, H. Shin, et al., "Selectivity in Chemiresistive Gas Sensors: Strategies and Challenges," *Chemical Reviews* 125 (2025): 4111–4183.

34. H. Zhang, Z. Zhang, Z. Li, H. Han, W. Song, and J. Yi, "A chemiresistive-potentiometric multivariate sensor for discriminative gas detection," *Nature Communications* 14 (2023): 3495.

35. P. Wang, Z. Shen, Y. Xia, et al., "Atomic Insights for Optimum and Excess Doping in Photocatalysis: A Case Study of Few-Layer Cu-$ZnIn_2S_4$," *Advanced Functional Materials* 29 (2019): 1807013.

36. J. Tan, X. Zhang, and Y. Huang, "Insights Into PMS Activation Mechanism by Te-Co_3O_4- for Levofloxacin Removal: Role of Interstitial and Substitutional Doping," *Chinese Chemical Letters* (2025): 112124, https://doi.org/10.1016/j.cclet.2025.112124.

37. S. Zhang, X. Dai, W. Hao, et al., "A First-Principles Study of the Nernst Effect in Doped Polymer," *Chinese Chemical Letters* 35 (2024): 109837.

38. A. Paul, B. Schwind, C. Weinberger, M. Tiemann, and T. Wagner, "Gas Responsive Nanoswitch: Copper Oxide Composite for Highly Selective H_2S Detection," *Advanced Functional Materials* 29 (2019): 1904505.

39. J. Cao, S. X. Tao, P. A. Bobbert, C.-P. Wong, and N. Zhao, "Interstitial Occupancy by Extrinsic Alkali Cations in Perovskites and Its Impact on Ion Migration," *Advanced Materials* 30 (2018): 1707350.

40. Q. Guo, J.-D. Zhang, J.-M. Liu, et al., "Promoting Charge-Carriers Dynamics by Relaxed Lattice Strain in A-Site-Doped Halide Perovskite for Photocatalytic H_2 Evolution," *Angewandte Chemie International Edition* 64 (2025): 202419082.

41. K. Li, H. Wang, Z.-K. He, Y.-Y. Song, Z. Gao, and C. Zhao, "Engineering Cl Vacancies in Lead-Free Halide Double Perovskites Decorated on TiO_2 Nanotubes for Highly Sensitive NO_2 Sensing at Room Temperature," *Chinese Chemical Letters* 36 (2025): 110610.

42. J. Pi, X. Jia, Z. Long, et al., "Surface and Defect Engineering Coupling of Halide Double Perovskite $Cs_2NaBiCl_6$ for Efficient CO_2 Photoreduction," *Advanced Energy Materials* 12: 2202074.

43. S. Wang, C. Tan, Q. Zong, et al., "Selective Reduction Laser Sintering: A New Strategy for NO_2 Gas Detection Based on In_2O_3 Nanoparticles," *Advanced Functional Materials* 35 (2025): 2419057.

44. X. Hu, B. Liu, H. Ma, et al., "Spatially Separated Molecular Activation Over Dual Sites in Sn-Doped $ZnGa_2O_4/SnO_2$ Photocatalysts Toward Complete VOCs Mineralization," *Advanced Sciences* (2025) 12: 09891.

45. X.-Y. Huang, K. Chen, W. Xie, et al., "Chemiresistive Gas Sensors Based on Highly Permeable Sn-Doped Bismuth Subcarbonate Microspheres: Facile Synthesis, Sensing Performance, and Mechanism Study," *Advanced Functional Materials* 33 (2023): 2304718.

46. Z. Zhou, J. Song, Y. Xie, et al., "DFT Calculation for Organic Semiconductor-Based Gas Sensors: Sensing Mechanism, Dynamic Response and Sensing Materials," *Chinese Chemical Letters* 36 (2025): 110906.

47. M. K. Salman, B. Karabay, L. C. Karabay, and A. Cihaner, "Elemental Sulfur-Based Polymeric Materials: Synthesis and Characterization," *Journal of Applied Polymer Science* 133 (2016): 43655.

48. W.-N. Zhao and Z.-P. Liu, "Mechanism and Active Site of Photocatalytic Water Splitting on Titania in Aqueous Surroundings," *Chemical Science* 5 (2014): 2256–2264.

49. C. E. Nanayakkara, J. Pettibone, and V. H. Grassian, "Sulfur Dioxide Adsorption and Photooxidation on Isotopically-Labeled Titanium Dioxide Nanoparticle Surfaces: Roles of Surface Hydroxyl Groups and Adsorbed Water in the Formation and Stability of Adsorbed Sulfite and Sulfate," *Physical Chemistry Chemical Physics* 14 (2012): 6957–6966.

50. C. Yang, Y. Wang, M. Liang, et al., "Towards Improving H_2S Catalytic Oxidation on Porous Carbon Materials at Room Temperature: A Review of Governing and Influencing Factors, Recent Advances, Mechanisms and Perspectives," *Applied Catalysis B: Environmental* 323 (2023): 122133.

51. T. Yang, M. Boepple, A. Hémeryck, et al., "H_2S Sensing With SnO_2 -Based Gas Sensors: Sulfur Poisoning Mechanism Revealed by Operando DRIFTS and DFT Calculations," *Angewandte Chemie International Edition* 64 (2025): 202504696.

52. Y. Han, Z. Yin, H. Zhuang, et al., "Synergistic Effects of Photoactivation and Photothermal in MXene Heterostructures for the Enhanced H_2S Detection Capability," *Advanced Functional Materials* 35 (2025): 09735.

53. X. Zhang, J. Zhao, H. Wang, et al., "MoO_2 Pump-Enhanced Flexible TiO_2 Nanojungle-Based Chemiresistors for Rapid Room-Temperature Detection of H_2S at Parts-Per-Billion Levels," *ACS Sensors* 8 (2023): 4179–4188.

54. J. Zhao, H. Wang, Y. Cai, J. Zhao, Z. Gao, and Y.-Y. Song, "The Challenges and Opportunities for TiO_2 Nanostructures in Gas Sensing," *ACS Sensors* 9 (2024): 1644–1655.

55. C. Szabo, C. Coletta, C. Chao, et al., "Tumor-Derived Hydrogen Sulfide, Produced by Cystathionine-β-Synthase, Stimulates Bioenergetics, Cell Proliferation, and Angiogenesis in Colon Cancer," *Proceedings of the National Academy of Sciences* 110 (2013): 12474–12479.

Supporting Information

Additional supporting information can be found online in the Supporting Information section.

Supporting File: adfm74089-sup-0001-SuppMat.pdf.